Received: 23 September 2019 | Revised: 5 June 2020 | Accepted: 17 June 2020

DOI: 10.1002/pip.3314

RESEARCH ARTICLE

PROGRESS IN PHOTOVOLTAICS WILEY

Absorber composition: A critical parameter for the effectiveness of heat treatments in chalcopyrite solar cells

Mohit Sood | Hossam Elanzeery | Damilola Adeleye | Alberto Lomuscio | Florian Werner | Florian Ehre | Michele Melchiorre | Susanne Siebentritt

Laboratory for Photovoltaics, Physics and Materials Science Research Unit, University of Luxembourg, Belvaux, L-4422, Luxembourg

Correspondence
Mohit Sood, Laboratory for Photovoltaics, Physics and Materials Science Research Unit, University of Luxembourg, L-4422 Belvaux, Luxembourg.
Email: mohit.sood@uni.lu

Funding information
Fonds National de la Recherche Luxembourg, Grant/Award Number: PRIDE/15/10935404; Luxembourgish Fonds National de la Recherche

Abstract

Post-device heat treatment (HT) in chalcopyrite [Cu (In,Ga)(S,Se)$_2$] solar cells is known to improve the performance of the devices. However, this HT is only beneficial for devices made with absorbers grown under Cu-poor conditions but not under Cu excess. We present a systematic study to understand the effects of HT on $CuInSe_2$ and $CuInS_2$ solar cells. The study is performed for $CuInSe_2$ solar cells grown under Cu-rich and Cu-poor chemical potential prepared with both CdS and Zn(O,S) buffer layers. In addition, we also study Cu-rich $CuInS_2$ solar cells prepared with the suitable Zn(O,S) buffer layer. For Cu-poor selenide device, low-temperature HT leads to passivation of bulk, whereas in Cu-rich devices, no such passivation was observed. The Cu-rich devices are hampered by a large shunt. The HT decreases shunt resistance in Cu-rich selenides, whereas it increases shunt resistance in Cu-rich sulfides. The origin of these changes in device performance was investigated with capacitance–voltage measurement, which shows the considerable decrease in carrier concentration with HT in Cu-poor $CuInSe_2$, and temperature-dependent current–voltage measurements show the presence of barrier for minority carriers. Together with numerical simulations, these findings support a highly doped interfacial p^+ layer device model in Cu-rich selenide absorbers and explain the discrepancy between Cu-poor and Cu-rich device performance. Our findings provide insights into how the same treatment can have a completely different effect on the device depending on the composition of the absorber.

KEYWORDS

composition, $CuInS_2$ solar cell, $CuInSe_2$ solar cell, defect passivation, efficiency, heat treatment, p^+ layer, quasi-Fermi level, time-resolved photoluminescence

1 | INTRODUCTION

The chalcopyrite Cu (In,Ga)(S,Se)$_2$ selenides and sulfides alloy system is a low-cost, non-toxic, and efficient thin-film photovoltaic technology, with Cu (In,Ga)(S,Se)$_2$ solar cells now at a record efficiency of 23.35%[1] and Cu (In,Ga)S_2 at 15.5%.[2] Further improvement in efficiency will depend critically on a deeper understanding of the role of limiting factors[3] such as recombination centers, which reduce the open-circuit voltage of the device.

In Cu (In,Ga)(S,Se)$_2$, post-device treatments have been traditionally investigated in terms of improving the open-circuit voltage (V_{oc}) and the fill factor (FF). These include a wide variety of treatments,

such as light soaking (LS),[4] heat treatment (HT) with[5] or without wet treatment,[6] combined heat LS (HLS) at different optimum temperatures,[7,8] and combined effect of heat and voltage bias soaking.[9] The optimum treatment and treatment conditions in each work are different and could be related either to the absorber composition or to the absorber/buffer (A/B)[7,10] interface.

The present work highlights the effect of absorber composition on the effectiveness of the post-device treatment. This was assessed by performing HT on both Cu-rich and Cu-poor absorbers with very different surface properties. Cu poor implies absorbers with a Cu/In ratio <1, and Cu rich implies absorbers grown under Cu excess, which consists of a stoichiometric $CuInSe_2$ phase and Cu selenide secondary phases.[11] The integral composition of the film shows a Cu/In ratio >1.

It has been reported that absorbers grown under Cu excess are characterized by larger grain size, lower potential fluctuation, better mobility, and lower defect density compared with Cu-poor absorbers.[12,13] However, solar cells based on absorbers grown under Cu excess suffer from lower efficiency compared with Cu-poor devices. This is mostly because they are dominated by interface recombination,[14] which can be traced to a Se-related defect, caused by the necessary etching process.[15] Therefore, to the present date, all the high-efficiency devices are realized by growing the absorbers with a final Cu-poor composition.[1,16,17] In all these Cu-poor devices, the dominant recombination path is in the bulk, rather than in the interface.[14] Therefore, it is worth performing an HT study using both Cu-poor and Cu-rich chalcopyrite absorbers, which have different dominant recombination paths and allow us to study the effect of annealing on the interface versus the bulk. Moreover, some of the best devices deploy sulfur to achieve favorable band bending at the front surface.[1,18] Therefore, it is important to also study the sulfide chalcopyrite.

In this contribution, we investigate the effects of HT on high-efficiency one-stage co-evaporated Cu-rich and Cu-poor $CuInSe_2$ and on Cu-rich $CuInS_2$ devices. Single-stage preparation of $CuInSe_2$ absorbers does not give us the best efficiencies, but we are aiming at comparable absorbers prepared by a similar process. Gallium-free absorbers are used to exclude any effects related to the Ga gradient. The devices were prepared with two different buffer layers: cadmium sulfide (CdS) and zinc oxysulfide [Zn(O,S)], to rule out buffer-related changes in device performance because of HT. We measure the effect of HT on the performance of these devices. The origin of the changes in device performance is investigated with capacitance–voltage (CV) measurement together with external quantum efficiency (EQE) and temperature-dependent current–voltage (JVT) measurements. For some absorbers, we include an in-depth study by photoluminescence (PL) quantum yield and lifetime measurements. Our findings provide insights into how the same treatment can have a completely different effect on the device depending on the composition of the absorber. Furthermore, while low-temperature HT (maximum 150°C) may slightly alter buffer layer properties, we do show that the HT has similar effects on the device properties independent of the buffer layer, as long as an appropriate band alignment[19] is ensured.

In this work, we first present the analysis of the effects of HT in the Cu-poor $CuInSe_2$ device prepared with the CdS and the Zn(O,S) buffer layers. We inspect and analyze the improvement in device performance and associate it to interface passivation and change in buffer composition. In the same section, we discuss the effects of the HT on Cu-rich $CuInSe_2$ and $CuInS_2$ solar cells. Further work is divided into four parts, always comparing Cu-poor to Cu-rich $CuInSe_2$ devices with a CdS buffer layer, plus $CuInS_2$ device with the better suited Zn(O,S) buffer layer. First, a direct comparison of the CV analysis of Cu-poor and Cu-rich devices is done. Whereas for Cu-poor devices, the apparent doping decreases with HT, for Cu-rich devices, it remains unchanged. Next, using PL as a tool, we discuss the impact of HT on the optical properties of Cu-poor and Cu-rich selenides. In Section 4, we discuss the JVT analysis of these devices, especially comparing Cu-poor and Cu-rich $CuInSe_2$ with Cu-rich $CuInS_2$, which provides insight into the observed differences and provides evidence for a surface with high defect density in the Cu-rich devices. Finally, in Section 5, to validate our assertions, numerical simulations are presented with a highly defective surface for Cu-rich $CuInSe_2$, which provides correspondence with our experimental results.

2 | PREPARATION AND TREATMENT OF SOLAR CELLS AND CHARACTERIZATION METHODS

Polycrystalline thin films of both $CuInSe_2$ and $CuInS_2$ absorbers were grown on a molybdenum-coated glass substrate. The $CuInSe_2$ absorbers were grown using a molecular beam epitaxy system, with a base pressure of 2×10^{-8} Torr in the chamber. Absorbers were made by a one-stage process by simultaneous co-evaporation of copper and indium metals on the substrates kept at a fixed temperature of 540°C in a selenium atmosphere. Different copper and indium fluxes were used to obtain "Cu-rich" and "Cu-poor" absorbers. The selenium flux was controlled using a valve cracker effusion cell. The growth of the Cu-rich $CuInS_2$ absorbers was done in a similar one-stage co-evaporation process at a constant process temperature of 590°C on molybdenum-coated high-temperature glass. It is to be noted that for $CuInSe_2$, we used soda–lime glass (SLG), whereas for $CuInS_2$, a high-temperature glass was used to avoid the temperature constraints posed by SLG due to its low melting point. The Na atomic % content in high-temperature glass is less than half the one in SLG, and the K atomic % content is more than an order of magnitude lower than SLG. We have to use higher temperatures for the sulfide absorbers because it was shown that temperature is a critical parameter for sulfide absorbers.[2,20] Otherwise, we try to keep the processes as similar as possible, in particular by using one-stage processes for all absorbers investigated. It must be noted that the $CuInS_2$ device grown on SLG also shows same trends in performance before and after HT as will be presented here with the high-temperature glass.

The elemental composition of unetched absorbers was measured using energy-dispersive x-ray spectroscopy (EDX) at 20 kV and is reported in Table 1. The values given represent an integral

TABLE 1 Chemical composition of the absorbers determined by energy-dispersive x-ray spectroscopy

	[Cu]	[In]	[Se] or [S]	[Cu]/[In]
Cu-poor $CuInSe_2$	24	26	50	0.92
Cu-rich $CuInSe_2$	30	22	48	1.36
Cu-rich $CuInS_2$	29	22	49	1.31

composition, including the Cu chalcogenide phases for Cu-rich films. After the absorber growth, the $Cu_{2-x}S/Se$ secondary phases[11] were removed using a 10% potassium cyanide (KCN) etching for 5 min in the case of Cu-rich absorbers. In the case of Cu-poor absorbers, a 5% KCN etching for 30 s was employed to remove oxides.

To make complete solar cells, the absorbers were further processed using either CdS or Zn(O,S) buffer layers by chemical bath deposition (CBD). For CdS buffer layer deposition, cadmium sulfate [$CdSO_4$] (2 mM), thiourea [CH_4N_2S] (50 mM), and ammonium hydroxide [NH_4OH] (1.5 M) in an aqueous solution at 67°C were used. For Zn(O,S), zinc sulfate heptahydrate [$ZnSO_4{\cdot}7H_2O$] (0.1 M), CH_4N_2S (0.4 M), and NH_4OH (2 M) in an aqueous solution at 84°C were used. The recipe for Zn(O,S) is adapted and modified from the literature report by Naghavi et al.[21] On top of the buffer layer, undoped zinc oxide (ZnO) and highly conductive aluminum-doped zinc oxide (Al:ZnO) window layers were sputtered before depositing Ni-Al contact grids using an electron beam evaporation. Finally, devices with an area of 0.4–0.5 cm^2 were identified using mechanical scribing. A list of all the devices investigated is reported in Table 2.

Device annealing at 100°C and 150°C was performed on a hot plate in the air on the same device sequentially. These two annealing steps will be referred to as HT1 and HT2. The HT was performed for 30 min in each case. After annealing, the sample was allowed to cool down to room temperature for 2 h.

Time-resolved PL (TRPL) measurements were performed to investigate the PL lifetime of the minority charge carriers in the $Mo/CuInSe_2/CdS$ stack before and after the HTs. The excitation was performed with a pulsed laser of 638-nm wavelength at a repetition rate of 200 kHz. The injection level was moderately high for the Cu-poor $CuInSe_2$ absorber, being on the same order as the estimated carrier concentration. However, for the Cu-rich $CuInSe_2$ absorber, the injection level was somewhat lower than the estimated carrier concentration. Although under high injection condition, the PL signal is proportional to Δn^2, contrary to Δn in the low injection condition, the excess carriers can still be monitored by the transient PL signal after low injection conditions have been established.[22] The integral PL signal near the band edge was measured. The lifetimes were extracted from the final slow long decay after the initial fast decay with a single exponential fit within one order of magnitude. The quasi-Fermi level splitting (qFls) is extracted from intensity calibrated and spectrally corrected PL spectra. Details can be found in the supporting information (data in SI) and in Babbe et al.[23]

TABLE 2 List of chalcopyrite absorber/buffer combination used in this study

Absorber	Growth condition	Absorber/buffer
$CuInSe_2$	Cu poor	$CuInSe_2/CdS$
		$CuInSe_2/Zn(O,S)$
	Cu rich	$CuInSe_2/CdS$
		$CuInSe_2/Zn(O,S)$
$CuInS_2$	Cu rich	$CuInS_2/Zn(O,S)$

The current–voltage (JV) characteristics of the produced solar cells were measured with a JV source measure unit using an AAA solar simulator with a Xenon short-arc lamp, calibrated with a Si reference cell. To perform the admittance and the JVT measurements, the samples were mounted in a closed-cycle cryostat under a base pressure below 4×10^{-3} mbar. For measuring the JVT, a cold mirror halogen lamp was used for illumination with an intensity equivalent to 100 mW/cm^2 by adjusting the height of the lamp from the sample to get the same J_{sc} as measured under the solar simulator. The conductance and the capacitance of the solar cell were recorded with an LCR meter for frequency in the range f = 20 Hz to 2 MHz with a controlled small-signal AC voltage pulse of 30 mV rms. To measure the sample temperature accurately, a Si-diode sensor was glued onto an identical glass substrate and placed just beside the solar cell. For numerical simulation, we used SCAPS1-D software developed at the Department of Electronics and Information Systems (ELIS) of the University of Gent, Belgium.[24]

3 | IMPACT ON OPTOELECTRONIC PROPERTIES OF SOLAR CELLS

In the following sections, we discuss the impact of HT on Cu-poor and Cu-rich chalcopyrite solar cells. The Cu-rich chalcopyrite devices are dominated by interface recombination,[12,14,15] whereas the Cu-rich chalcopyrite devices are not dominated by interface recombination.[14] For the Cu-poor $CuInSe_2$ devices, we observe the passivation of bulk defects with both HTs, as evident from the improvement in open-circuit voltage, lifetime, and qFls of the absorber. The main additional effect of HT2 is a decrease in doping, which improves the short circuit current. For the Cu-rich $CuInSe_2$ device, no passivation of defects is observed, as the lifetime does not change with any HT. Changes in qFls can be fully explained by the observed small changes in the doping level. The V_{oc} decreases due to a deterioration of device shunt with HT1 and HT2 and due to the degradation of contact layers after HT2, as evidenced by a large difference between V_{oc} and qFls. Finally, for the Cu-rich $CuInS_2$, all changes can be traced back to changes in the shunt resistance.

3.1 | Device performance

We start by discussing the HT effects on Cu-poor selenide devices with different buffers. Figure 1A,B shows the summary of the device performance before and after the two HTs for devices with the CdS and Zn(O,S) buffer layers.[14] With the HT1, for both device structures,

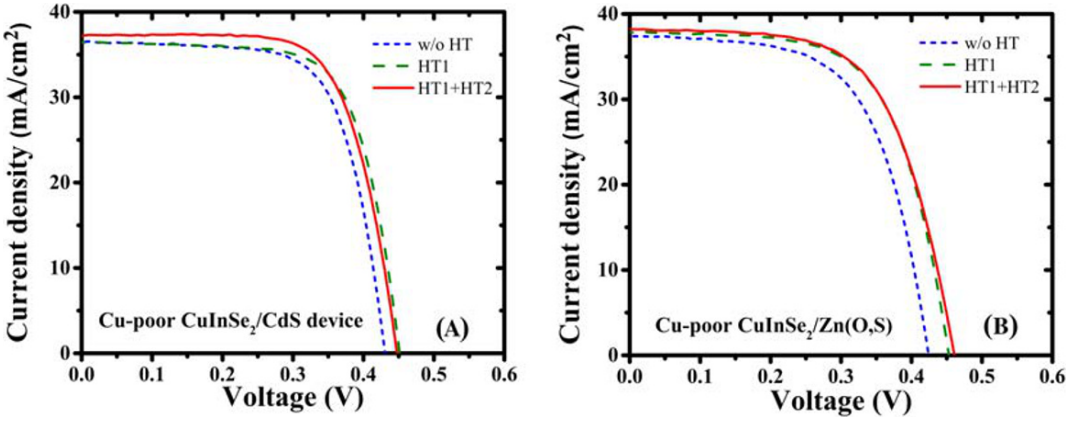

FIGURE 1 Current–voltage characteristics of Cu-poor $CuInSe_2$ device before and after the two HTs with (A) CdS buffer layer and (B) ZnOS buffer layer. HT, heat treatment [Colour figure can be viewed at wileyonlinelibrary.com]

we see an increase in the device efficiency, largely due to the improvement in V_{oc} and small improvement of FF in the case of the Zn(O,S) buffer. Further, the HT2 does not result in a considerable change in device parameters, and the device efficiency remains almost unchanged. To understand the origin of these improvements after the HT, the JV curve is fitted (Figure S1) with one diode model to extract the ideality factor (A) and the saturation current (J_o). Fitting was done by the JV fit method[25] using a Python script developed in our lab, based on orthogonal distance fitting. The fit results along with the device JV parameters for the dark curve are presented in Table 3.

We will start by discussing the impact of HTs on the device V_{oc}. After HT1 the saturation current (J_o) decreases in both devices (Table 3), as a consequence, we see an improvement in V_{oc} by ~20–30 mV. The HT2 has a different impact on the recombination in each device. For the $CuInSe_2$/CdS device, it leads to a decrease in J_o and the ideality factor (A), whereas for the $CuInSe_2$/Zn(O,S) device, both J_o and A increase. In both cases, the combination of changes in J_o and A leaves the V_{oc} almost unchanged. We will later show that in the CdS buffered device, HT2 leads to a change in doping level and the carrier lifetime, which may explain the changes in J_o and A. However, the changes are minor in both cases and might not be attributable to a single cause. Although it is not so obvious here, later in Section 3.3 with the help of TRPL and qFls measurements, we will show evidence favoring the passivation of absorber and interface/contacts after each HT.

The minute improvement in FF after HT1 originates from the increased V_{oc} of the devices. In the $CuInSe_2$/Zn(O,S) device, HT2 increases the series resistance of the device (Table 3), which reduces the FF.

To understand the increase in J_{sc} in both devices after HT2, we investigate the EQE of both devices. Figure 2A shows the EQE spectrum of the $CuInSe_2$/CdS device before and after HT1 + HT2; there is an improvement in EQE of the device in the long-wavelength region. This is a direct result of increased carrier collection of the carriers generated far from the junction, as the space charge region (SCR) width increases after HT due to reduced doping of the absorber. This change of SCR width is observable in capacitance measurements and will be discussed later. The $CuInSe_2$/Zn(O,S) device also shows an improvement in the EQE after HT1 + HT2 (Figure 2B), unlike the $CuInSe_2$/CdS the improvement in this case is in the entire wavelength spectrum. Even though the SCR width also increases in this device after HT, it is not enough to improve the EQE. The increase in the EQE is completely dominated by the decreased reflectance of the light in the structure (see inset Figure 2B).

We now discuss the results for the Cu-rich $CuInSe_2$ and $CuInS_2$ solar cells. For $CuInSe_2$, we used the CdS buffer layer to complete the solar cell, whereas for $CuInS_2$, we used Zn(O,S) as a buffer layer, as CdS does not have optimum band alignment with $CuInS_2$.[10,26,27] The JV curve of the devices before and after HT1 and HT2 is shown in Figure 3. Both one-stage Cu-rich $CuInSe_2$ and $CuInS_2$ solar cells have

TABLE 3 Device parameters of best Cu-poor $CuInSe_2$ device prepared with CdS and ZnOS buffer layer before and after the HTs, extracted from the current–voltage characteristics, from fit to dark current–voltage characteristics

Cu poor	Efficiency (%)	V_{oc} (mV)	J_{sc} (mA/cm^2)	FF (%)	A	J_o (mA/cm^2)	R_{sh} (ohm-cm^2)	R_s (ohm-cm^2)
$CuInSe_2$/CdS no HT	10.8	430	36.5	69	1.34	8.4×10^{-5}	732	0.3
$CuInSe_2$/CdS HT1	11.5	451	36.5	70	1.34	4.8×10^{-5}	795	0.3
$CuInSe_2$/CdS HT2	11.5	447	37.2	70	1.24	1.8×10^{-5}	2818	0.4
$CuInSe_2$/ZnOS no HT	9.8	424	37.4	62	1.84	3.2×10^{-3}	706	0.3
$CuInSe_2$ZnOS HT	10.8	453	37.4	64	1.88	2.3×10^{-3}	846	0.4
$CuInSe_2$/ZnOS HT2	10.9	460	38.1	62	2.06	4.3×10^{-3}	1092	0.6

Abbreviations: FF, fill factor; HT, heat treament.

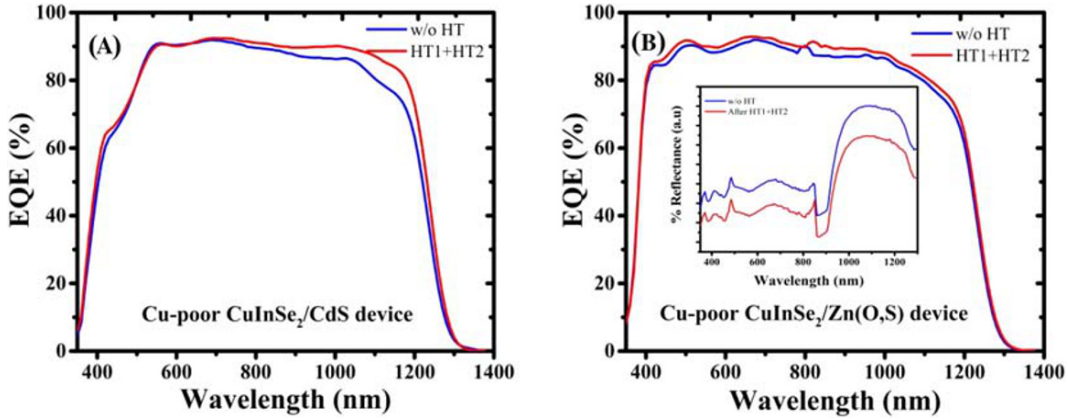

FIGURE 2 External quantum efficiency (EQE) versus wavelength spectrum for Cu-poor $CuInSe_2$ with (A) CdS buffer layer and (B) with Zn(O,S) buffer layer before and after HT1 + HT2. The inset in (B) represents the reflection measurements with and without HT1 + HT2. HT, heat treatment [Colour figure can be viewed at wileyonlinelibrary.com]

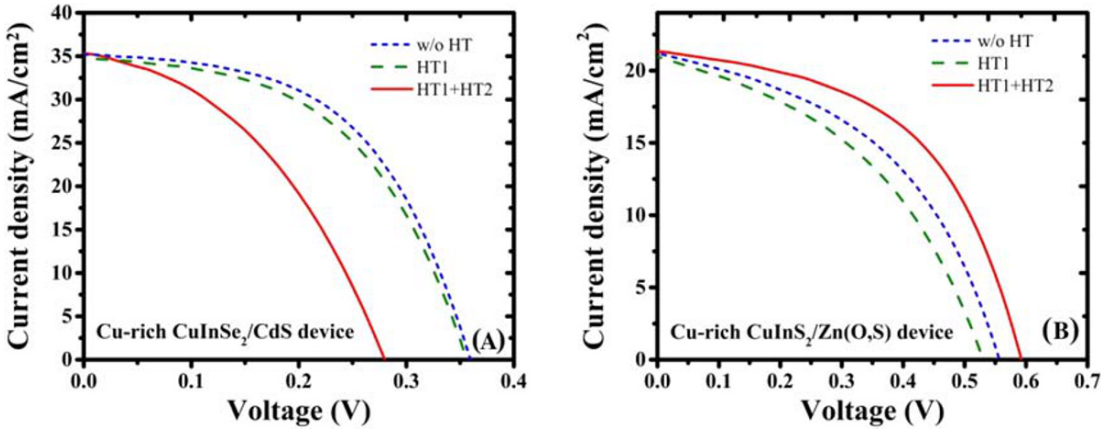

FIGURE 3 Current–voltage characteristics of (A) Cu-rich $CuInSe_2$ device with CdS buffer and (B) Cu-rich $CuInS_2$ device with ZnOS buffer layer before and after the two HTs. HT, heat treatment [Colour figure can be viewed at wileyonlinelibrary.com]

low R_{sh} (Table 4 and Figure S2, determined from the inverse of the slope of the JV curve in slight reverse bias, i.e., from −0.1 to 0.0 V), which makes a one-diode fit completely unreliable. Although, after etching, the Cu/In ratio is ~1 and we do not see any indication of secondary phases in x-ray diffraction (XRD) or Raman, we cannot fully exclude the presence of traces of Cu_xSe_y and Cu_xS_y phases in our absorbers after etching. It has been reported[28,29] that grain boundaries in Cu-rich absorbers show Cu accumulation together with traces of $Cu_{2-x}S/Se$, which might be one of the reasons for large shunting pathways in Cu-rich devices.

Unlike Cu-poor $CuInSe_2$ devices, the Cu-rich $CuInSe_2$ device performance decreased slightly after HT1 (Figure 3A). This is mostly due to a loss in FF, which is at least partly due to the decrease in the already low R_{sh} (Table 4). The device shunt became even worse after HT2, leading to further deterioration of the FF. In addition, the V_{oc} also decreases substantially, much more than the qFls, as we will

TABLE 4 Device parameters of best Cu-rich $CuInSe_2$ device prepared with CdS and best Cu-rich $CuInS_2$ device prepared with ZnOS before and after the HTs

Cu rich	Efficiency (%)	V_{oc} (mV)	J_{sc} (mA/cm^2)	FF (%)	R_{sh} (Ω-cm^2)	R_s (Ω-cm^2)
$CuInSe_2$/CdS	6.7	360	35.2	53	200	0.4
$CuInSe_2$/CdS HT1	6.4	356	35.2	51	162	0.4
$CuInSe_2$/CdS HT2	4.1	280	35.4	41	80	0.3
$CuInS_2$/ZnOS	5.3	556	21.1	45	100	0.1
$CuInS_2$/ZnOS HT1	4.6	530	20.9	42	85	0.1
$CuInS_2$/ZnOS HT2	6.4	592	21.3	51	199	0.2

Abbreviations: FF, fill factor; HT, heat treament.

discuss later, indicating a deterioration in the buffer/window (B/W) layers. Thus, the device efficiency decreases from 6.7% to 4.1%. The different results of HT on Cu-rich and Cu-poor $CuInSe_2$ can be explained by variations in the defect chemistry,[30] which depends upon the chemical potential of constituents and final composition, even though the absorbers were grown by a similar deposition process. Furthermore, the necessary etching process for the Cu-rich absorbers leads to a p^+ layer near the junction, as we will discuss later, which influences the reaction to the HT. This confirms the crucial role of the absorber composition on the electronic properties and defect formation energy.

In the case of Cu-rich $CuInS_2$, we observed degradation in the device performance from 5.3% to 4.6% after HT1. This decrease is due to lower V_{oc}, which is a result of a reduction in R_{sh}. However, the HT2 results in an increase of R_{sh}, and consequently, both V_{oc} and FF improve (Table 4). As a net result of this, we get an improved device efficiency from 4.6% to 6.4%. This trend is opposite to Cu-rich $CuInSe_2$ solar cell. Although both absorbers ($CuInS_2$ and $CuInSe_2$) were grown in the one-stage process, the effect of HT is completely different in both cases. The changes are largely due to changes in the shunt; however, the trends after HT2 are opposite. This indicates how two closely related alloys grown in an almost same chemical potential window can have significantly different electronic structures, possibly mostly at the grain boundaries. This might be due to the preparation of $CuInS_2$ with Zn(O,S) buffer layer and the $CuInSe_2$ device prepared with the CdS buffer layer. However, we rule out the impact of different glass substrates, as the $CuInS_2$ devices prepared on SLG also show an increase in device efficiency with HT2 (not shown here).

Although in this section, we looked at the impact of HT1 and a combination of HT1 + HT2 on device efficiency, it must be noted that the impact of HT2 alone on the device without HT1 results in similar device efficiency trends as for HT1 + HT2 (Table S1).

3.2 | Effect of HT on doping density

To ascertain the change in apparent doping and SCR width after annealing in the $CuInSe_2$ devices, the CV measurements were performed before and after annealing. The SCR width in Table 5 is extracted from capacitance at ~0.2 V at 100 kHz by

$$w = \varepsilon\varepsilon_o A/C, \quad (1)$$

where C is the capacitance, w is the SCR width, ε is the relative dielectric permittivity of absorber, and ε_o is the dielectric permittivity of free space. For calculations, we have used a value of ε equal to 10, as is often used in literature.[31,32] This SCR width does contain contributions from the buffer layer.[33,34] We therefore discuss only changes and not the absolute values. For the same reason, we use the label "apparent" for the doping density and the depth inside the absorber. The apparent carrier concentration for Cu-poor device is calculated using the local derivative in forward bias ~0.2 V in the Mott–Schottky plot. The detailed methodology is described in the supporting information. Figure 4A shows the doping profile before and after the two HTs for Cu-poor $CuInSe_2$. The CV measurements clearly show a decrease in apparent doping and an increase in the SCR width after HT2. Although there is no major change in the apparent doping for HT1, the apparent doping decreases by one order of magnitude (from 10^{16} to 10^{15} cm^{-3}) after the HT2. Also, the SCR width increases from 240 to 890 nm before and after HT2. A similar trend is observed for a device with Zn(O,S) buffer layer (Figure S3). The prominent reason for the decrease of carrier concentration after HT2 may be the diffusion of extrinsic chemical species (cadmium/zinc) into the $CuInSe_2$ absorber, which has been reported to reduce carrier concentration in earlier reports.[35–41] Both zinc and cadmium have been calculated to form Zn_{Cu} and Cd_{Cu} shallow donor defects using first-principle methods,[42] which results in a decrease of net p-type doping in $CuInSe_2$. Another feature of this doping profile of Cu-poor $CuInSe_2$ is the "U" shape. This shape is due to high apparent doping towards the front and back part of the junction. The increase in apparent doping towards the front is attributed to minority carrier injection at high forward bias, whereas the increase towards the back could be due to a contribution from the deep defects[40,43] or the bulk doping at the back of the absorber, unaffected by buffer (i.e., Cd or Zn) diffusion.[41]

The CV analysis of Cu-rich $CuInSe_2$ shows higher apparent doping compared with Cu-poor $CuInSe_2$ (Figure 4B). This has been observed previously.[12,44] The apparent doping is particularly high near the surface of the absorber; however, the absorber apparent doping decreases going from surface to the bulk. This high apparent doping at the surface of Cu-rich $CuInSe_2$ device is partly due to a Se-related acceptor defect as reported in Elanzeery et al.[15] After HT1, the

TABLE 5 Device apparent doping and apparent SCR width of Cu-poor $CuInSe_2$ device prepared with CdS and ZnOS buffer layer before and after the HTs

Cu poor	SCR (nm)	N_A (cm^{-3})	Cu rich	SCR (nm)	N_A (cm^{-3})
$CuInSe_2$/CdS no HT	178	1.1×10^{16}	$CuInSe_2$/CdS	132	4.2×10^{16}
$CuInSe_2$/CdS HT1	226	9.8×10^{15}	$CuInSe_2$/CdS HT1	141	4.4×10^{16}
$CuInSe_2$/CdS HT2	775	6.0×10^{14}	$CuInSe_2$/CdS HT2	167	3.0×10^{16}
$CuInSe_2$/ZnOS no HT	123	2.0×10^{16}	$CuInS_2$/ZnOS	59	3.0×10^{17}
$CuInSe_2$ZnOS HT	149	1.3×10^{16}	$CuInS_2$/ZnOS HT1	60	3.0×10^{17}
$CuInSe_2$/ZnOS HT2	208	5.2×10^{15}	$CuInS_2$/ZnOS HT2	58	3.6×10^{17}

Note. Also included is the apparent doping and apparent SCR width for Cu-rich $CuInSe_2$ and $CuInS_2$ devices prepared with CdS and ZnOS, respectively, before and after the HTs, extracted from capacitance–voltage measurements.
Abbreviations: HT, heat treatment; SCR, space charge region.

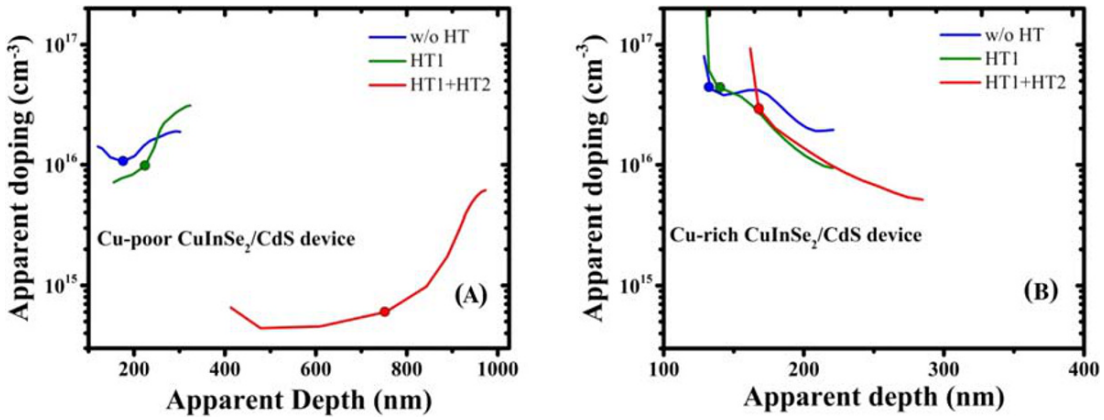

FIGURE 4 Apparent doping profile versus apparent depth for (A) Cu-poor $CuInSe_2$ and (B) Cu-rich $CuInSe_2$ before and after the HT1 and HT2 with the CdS buffer layer. The dot represents the value of apparent depth and apparent doping measured using the local derivative at forward bias ~0.2 V in the Mott–Schottky plot. Please note the difference in the x-axis scales on two curves. HT, heat treatment [Colour figure can be viewed at wileyonlinelibrary.com]

apparent doping does not change, similar to Cu-poor $CuInSe_2$. Finally, with HT2, we observe a small decrease in absorber doping; however, the overall doping profile remains very similar to the unannealed device, suggesting only a very slight change in the absorber doping even after HT2. The fact that HT does not lead to a substantial decrease in doping, as in the case of Cu-poor $CuInSe_2$, explains why we do not see the improvement in J_{sc} after HT2 in Cu-rich $CuInSe_2$ solar cells.

A similar observation is made for Cu-rich $CuInS_2$ solar cells (see Figure S4). In $CuInS_2$ also, HT has no significant effect on the doping profile of the absorber. The most probable cause for this in Cu-rich devices might be the low concentration of Cu vacancies in the absorber. As a result, the Cd or Zn does not have enough sites to diffuse into the absorber.[45] Another reason may be the highly defective surface layer in Cu-rich absorbers,[15] which can also reduce the diffusion of Cd and Zn. We will discuss the nature of this layer later. In summary, whereas in Cu-poor devices, the diffusion of Cd or Zn chemical species results in the decrease of the absorber carrier concentration after HT2, in Cu-rich $CuInSe_2$ or $CuInS_2$ device, we do not see any major change in the doping concentration.

3.3 | Impact on optical properties

To understand the effects of HT on Cu-poor and Cu-rich selenides, in this section, we will examine their optical properties using PL spectroscopy. Due to poor PL signal, the Cu-rich sulfides will not be included in this section. The changes in non-radiative recombination in Cu-poor selenides after HTs can be the result of either change in the bulk of the absorber or interface of the device or both. Hence, to identify the root cause of this change, we performed qFls and TRPL measurements on the Mo/$CuInSe_2$/CdS stack before and after the two HTs. The deduced values of the qFls for Cu-poor $CuInSe_2$ are presented in Figure 5A. The entire procedure of extracting qFls can be found in the supporting information and in Figure S5. Before the HTs, the qFls was evaluated to be 454 meV. After HT1, the qFls was increased to 473 meV (+19 meV). In contrast, after HT2, the value reduced back to 455 meV (unchanged with respect to the untreated absorber). These changes in qFls could originate from the change in carrier concentration as[46]

$$\Delta \mathrm{qFls} = kT \ln\left(\frac{N_A}{N_{Ao}}\right), \tag{2}$$

where k is Boltzmann constant, T is the temperature, N_A is the net majority carrier concentration after either of the HTs, and N_{Ao} is the majority carrier concentration before HT. The calculated ΔqFls from Equation 2 using the apparent majority carrier concentration from Table 5, before and after HT1 and before and after HT2, comes out to be −3 and −75 meV, respectively. This predicted change is much smaller than the measured qFls change after HT1 and more negative than the measured qFls change after HT2 with respect to the untreated case. Hence, changes in qFls cannot be explained by the change in N_A alone, and therefore, the lifetime (τ) must also change. Figure 5C depicts the measured TRPL decay of Cu-poor $CuInSe_2$ before and after the HTs. The lifetime increases continuously with every HT, reaching a nearly double value after HT2 compared with the untreated absorber. The longer lifetime after the HT indicates that there is a reduction in non-radiative recombination loss,[22] as recombination centers reduce minority carrier lifetime. These results together with device characteristics (Table 3) suggest that HT1 leads to qFls increase and, as a consequence, an equivalent increase in V_{oc}, suggesting the passivation of recombination centers in the absorber. This passivation is most probably caused by the diffusion of chemical species from the buffer into the absorber. After HT2, the lifetime increases further; this explains the lower decrease in qFls compared with the one calculated just by carrier concentration changes (72 meV expected due to decrease in doping). In addition, there is also a lower deficit between the qFls and V_{oc} after HT2 (Table 3); this observation indicates the passivation of the interface/contacts in addition to the absorber.

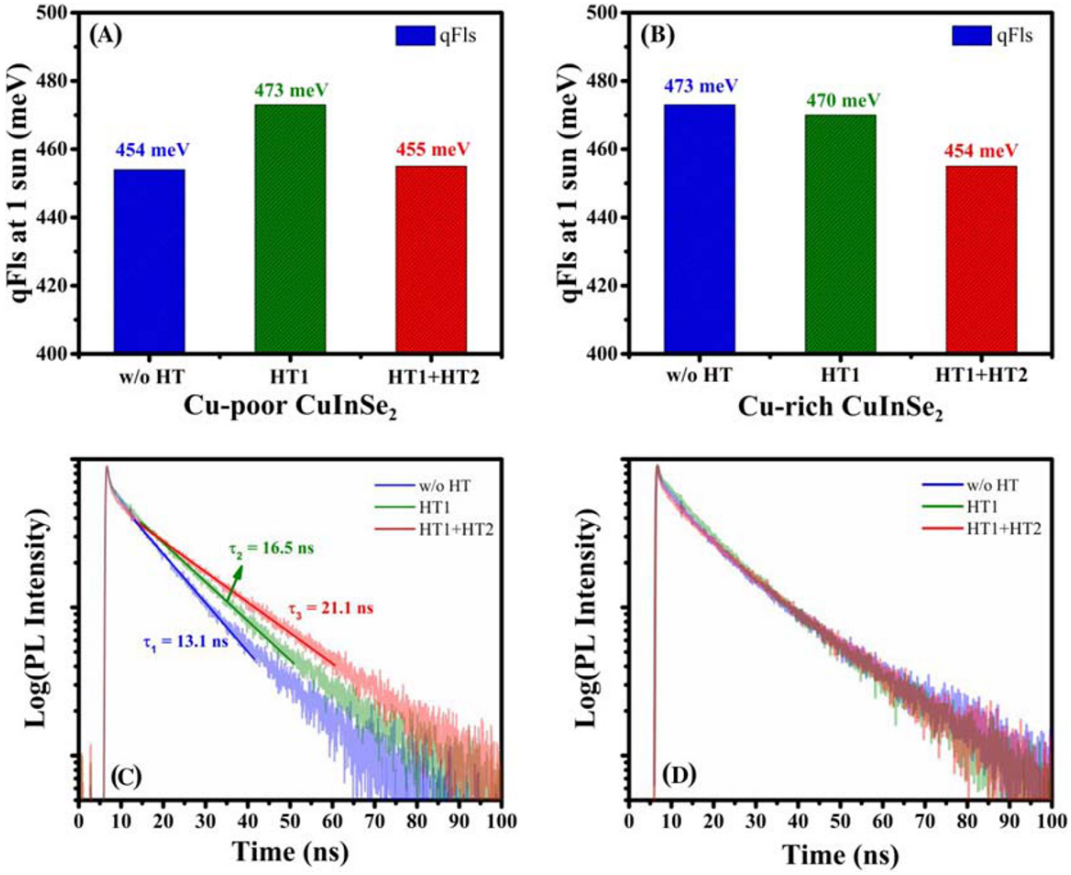

FIGURE 5 Quasi-Fermi level splitting (qFls) at 1 sun of the Mo/$CuInSe_2$/CdS stack before and after the two HTs for (A) Cu-poor $CuInSe_2$ absorber and (B) Cu-rich $CuInSe_2$ absorber and logarithm of the normalized time-resolved photoluminescence (TRPL) measurements curve for (C) Cu-poor $CuInSe_2$ absorber and (D) Cu-rich $CuInSe_2$ absorber. The effective lifetime of minority carriers was extracted from the final slow long decay after the initial fast decay with a single exponential fit. HT, heat treatment; PL, photoluminescence [Colour figure can be viewed at wileyonlinelibrary.com]

We now discuss the impact of HT on the qFls and TRPL values for Cu-rich $CuInSe_2$. Figure 5B shows the qFls values after HT1 and HT2. Only HT2 results in a significant decrease in the qFls, from 473 meV before HT to 454 meV after HT2. This value is very close to the ΔqFls, calculated from Equation 2 (10 meV) using majority carrier concentrations (from Table 5) for the device before and after HT2. For HT1, the calculated ΔqFls is 2 meV, nearly equal to the difference of the qFls measured by calibrated PL. In contrast to the Cu-poor device, the minority carrier lifetime evaluated (15 ± 2 ns) does not change for Cu-rich device (Figure 5D). This explains why the Cu-rich device performance does not improve after HT1 or HT2, as neither qFls nor lifetime improves. The higher difference between the V_{oc} and qFls after HT indicates a degradation of the B/W layers, leading to an additional gradient in the electron quasi-Fermi level and hence lower V_{oc} in the device.

4 | JVT ANALYSIS

JVT analysis is an important characterization technique that can help to understand the carrier transport and recombination dynamics in the device. In this section, we will discuss the JVT curves of the Cu-poor and Cu-rich $CuInSe_2$ device with the CdS buffer layer and Cu-rich $CuInS_2$ device with the Zn(O,S) buffer layer, before and after HT.

In all the JV curves, we observe that the superposition principle is not valid: the dark and light JV curves cross each other. The crossing becomes more prominent after HT as seen in Figure 6. Under ideal circumstances (i.e., device has a similar behavior under dark and illumination), a moderate conduction band (CB) barrier (<0.4 eV)[19] should not result in JV crossover. However, in the buffer layer, a phenomenon known as "photodoping" has been observed.[47,48] This is mostly explained by an increase in the free carrier concentration in the material upon illumination and the release of free electrons from the deep acceptor levels in CdS[49] or from a thin ordered defective layer near the interface[32] (the latter is not observed in our case; see Raman spectra, Figure S6). Thus, the photodoping of the buffer, together with the CB spike at the A/B interface and CB cliff at the B/W interface,[48,50,51] can explain the JV crossover. In the following, we discuss first the cause of the crossover for the example of the standard Cu-poor $CuInSe_2$ device.

To investigate the origin of the photodoping in our case, we performed JV measurement under illumination with the red light at

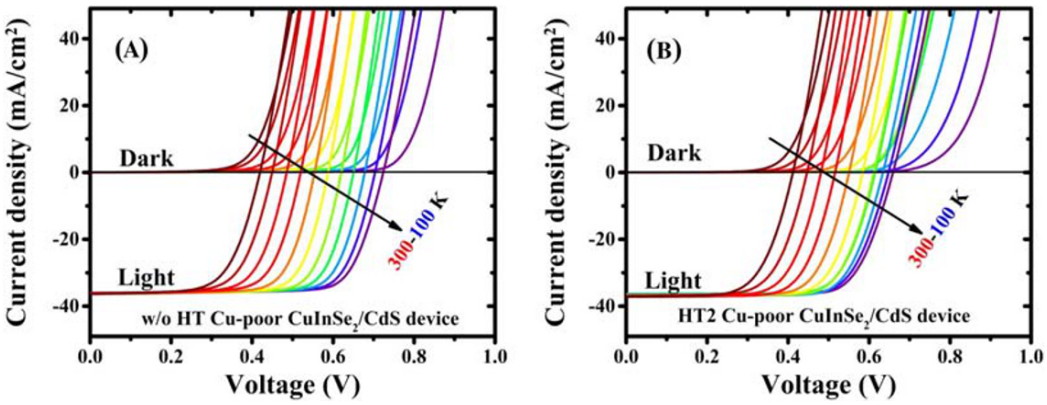

FIGURE 6 Temperature-dependent current–voltage curves of Cu-poor $CuInSe_2$ device made with CdS buffer layer under dark and illumination condition (A) before HT and (B) after HT1 + HT2 showing more pronounced crossover. HT, heat treatment [Colour figure can be viewed at wileyonlinelibrary.com]

660-nm wavelength, to excite carriers deep inside the absorber. The measurements were done in the cryostat at 205 K, where the crossover (with white light, see yellow curve, Figure 6A) is very prominent and visible. To inject the same amount of carriers into the junction, we fix the red LED intensity to obtain the same J_{sc} as with the halogen lamp. The JV curve of the device with 1 sun equivalent halogen lamp and 1 sun equivalent red LED has essentially the same crossover point (Figure S7). This measurement reveals that it is not the direct generation of the carriers in the CdS buffer under illumination that causes this photodoping, rather it is the injection of carriers from the absorber into the buffer. Hence, the crossover is most likely due to carriers generated in the absorber close to the interface and not due to the carrier generation in the buffer itself.

The crossover and its temperature dependence can be understood by assuming thermionic emission transport across the barrier at the A/B interface. According to thermionic transport model, the current across the barrier is given by[52]

$$J_n \approx A^* T^2 e^{-\frac{\varphi}{kT}}. \quad (3)$$

φ is the barrier height, which in this case, $\varphi = E_c - E_{fn}$, as shown in Figure 7, where E_c is the minimum of the CB edge at the buffer absorber interface and E_{fn} is the electron quasi-Fermi level at the interface, and $A^* = (4\pi q m^* k^2/h^3)$ is the modified Richardson constant and T is the temperature. Now under dark conditions at sufficient forward bias $>V_{oc,}$ the barrier is active and has a certain value (Figure 7A) that an electron has to overcome to travel across the interface into the absorber. As a result, there is a small potential drop across the interface. However, due to the increase of electron concentration in the buffer under illumination, the barrier is reduced (Figure 7B), and as a result, the potential drop across the interface is less than in the dark. This leads to the crossover of light and dark JV curves as can be seen in Figure 6. This effect is demonstrated by device simulations in Section 5.

The temperature dependence of the crossover can be understood by the following: considering a constant barrier, the thermionic current is smaller at a lower temperature. Therefore, the current at which the effect of the different barriers in dark and light matters becomes lower. This shifts the crossover points to lower currents and higher voltages.The crossover effect is more pronounced in the device with HT2 as observed in Figure 6B, that is, the current at the crossover point is lower. This can be due to the increase of Cu diffusion into the CdS causing the dark carrier concentration of the CdS to decrease even more and eventually resulting in an even higher barrier in the dark.The behavior of the JVT characteristics (Figure S8) for the Cu-rich $CuInSe_2$ device before any HT and after HT2 is similar to the one

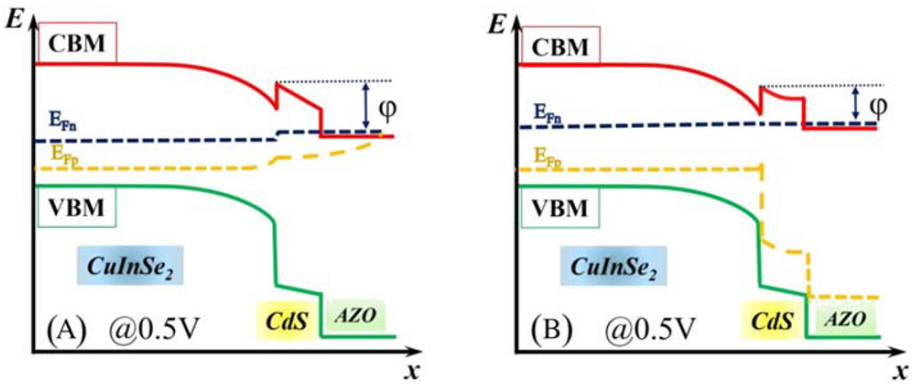

FIGURE 7 Band diagram of $CuInSe_2$ device at a forward bias of 0.5 V along with the fermi level under (A) dark and (B) illuminated condition. Here, AZO is Al-doped ZnO, the transparent conducting oxide window. One can visualize the lowering of barrier height φ under illumination [Colour figure can be viewed at wileyonlinelibrary.com]

in the Cu-poor $CuInSe_2$ devices: it also shows pronounced crossover between JV under dark and illumination at all temperatures in HT device and at lower temperatures in untreated device. In addition to this, the JVT curves show a peculiar feature that is not observed for the Cu-poor $CuInSe_2$ device. At lower temperatures, around 150 K, the forward dark current of the untreated device tends to flatten at moderate voltages ~0.4 V (Figure S8a). A rollover is observed for the same device under illumination (Figure 8A) at lower temperatures (<150 K). After HT2, however, the forward dark current becomes more exponential with voltage compared with the unannealed device (Figure S8b). Furthermore, no rollover is observed for the HT2 device under illumination. This can be most clearly seen in Figure 8B where we compare the illuminated JV characteristics at low temperature for annealed and unannealed devices. In the following, we trace back this behavior to the reduction of a p^+ layer in the Cu-rich devices.

We have recently shown that in Cu-rich $CuInSe_2$, after strong KCN etching, we form deep defects near the interface.[15] Plus, it has been argued that this defect is an acceptor defect and causes the carrier concentration gradient in the $CuInSe_2$ absorber layer with high doping (p^+) towards the front surface. As a result, we form a p-p^+-n device structure, and in the energy band diagram under equilibrium conditions, an additional barrier forms near the surface of the absorber (see Figure 9). The impact of the properties of the p^+ layer on device JV rollover has been studied in detail by Maciaszek.[53] In this report, for simulations, a carrier concentration of 3×10^{17} cm^{-3} was used for the p^+ layer, which is much higher than the calculated values (2×10^{16} to 4×10^{16} cm^{-3}, Table S2) for the Cu-rich $CuInSe_2$ devices discussed here. In addition, for simplicity, no CB offset (CBO) at any of the interfaces was considered in their work. But in a realistic scenario, in the device structure, there are band offsets at the different interfaces, namely, A/B and B/W interface.[54–56] The energy band diagram in such a case is depicted in Figure 9. It is evident that in addition to the p^+ layer for the photogenerated electrons, there is an additional barrier at the A/B interface due to the CB spike. Similarly, for injected electrons at high forward voltage, that is, above V_{oc}, there are again two active barriers: one due to p^+ layer as considered in the report by Maciaszek[53] and the other one due to CBO at B/W interface. This combination of two barriers causes the rollover as observed in Figure 8A in our case with much lower doping in the p^+ layer, than assumed by Maciaszek. It is known that even in Cu-rich Cu (In,Ga)Se_2,

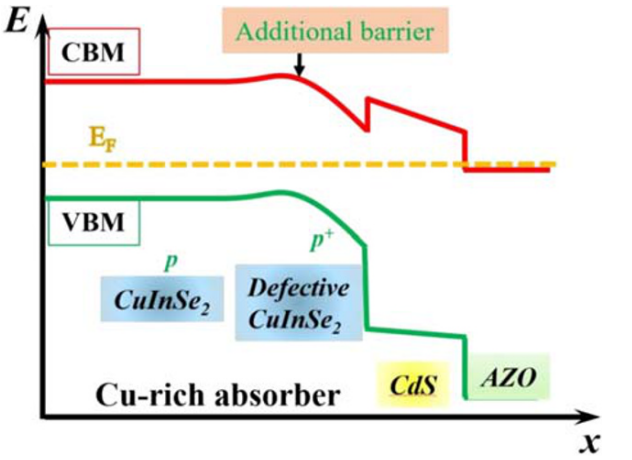

FIGURE 9 Energy band illustration of a device structure with p^+ layer near absorber/buffer interface [Colour figure can be viewed at wileyonlinelibrary.com]

annealing causes cadmium diffusion into the absorber (albeit significantly lower than in Cu-poor ones).[39] Another potential effect is the outdiffusion of sodium (Na) from the bulk to the surface[57] after annealing. We speculate that either of these species (Cd or Na) partially removes or compensates the acceptor-like defect near the absorber surface. The reduction in p-type doping is evident from the CV measurements (Figure 4B) where the equilibrium apparent doping decreases from 4×10^{16} to 3×10^{16} cm^{-3} after HT2 due to partial passivation or compensation of the acceptor defect (see discussion supplement and Figure S9). Furthermore, the strong increase of the apparent doping near the surface of the absorber (low apparent depth in Figure 4B) is reduced after HT2. This reduction in doping concentration lowers the barrier due to the p-p^+ layer at the front, and consequently, one no longer sees the double diode or the rollover effect (Figure 8B) at lower temperatures for HT2 device. We must emphasize here that even though the p^+ layer is partially passivated by HT2, the device performance becomes worse. This can be understood by two observations, discussed above: (i) the lifetime does not increase, indicating that the observed lifetime depends mostly on recombination centers in the bulk, outside the p^+ layer, and (ii) the difference between qFls and V_{oc} increases dramatically, due to contact layer degradation, which overcompensates any positive effect of the passivation of the p^+ layer.

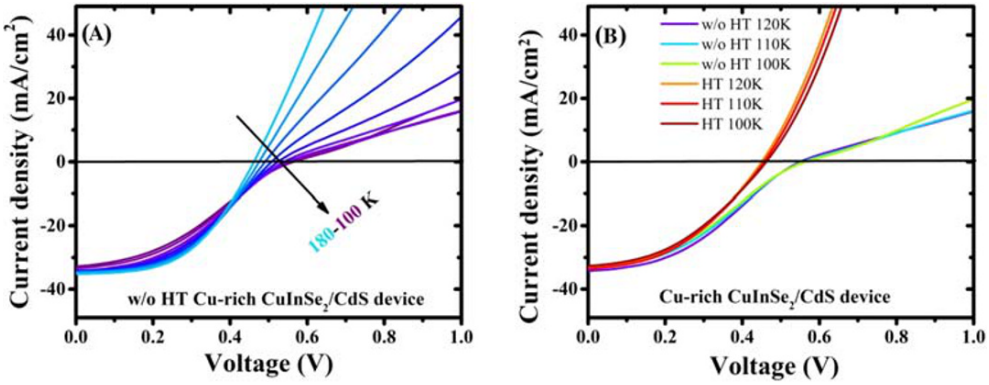

FIGURE 8 Illuminated temperature-dependent current–voltage curves of Cu-rich $CuInSe_2$ at (A) 180–100 K before HT and (B) 120–100 K before and after HT1 + HT2. The curves show the rollover in the device without HT and removal of the rollover effect after HT. HT, heat treatment [Colour figure can be viewed at wileyonlinelibrary.com]

In the case of $CuInS_2$ device, unlike $CuInSe_2$, neither the flattening of dark JVT curve nor the rollover effect in illuminated JVT curve at forward bias is observed for the device in Figure 10. Therefore, JVT does not provide sufficient evidence for the presence of the p^+ layer in the sulfide absorber in this device. However, there can still be a p^+ layer in the Cu-rich $CuInS_2$ device. As our numerical simulations (Section 5) prove, the rollover in the JVT depends not only on the presence of the p^+ layer but also on the CBO at the B/W interface. We do find evidence for a p^+ layer in Cu-rich sulfide absorbers: we investigate a similar one-stage $CuInS_2$ absorber but equipped with an alternative Zn(O,S) buffer. This alternative Zn(O,S) is deposited by a different CBD recipe and has lower oxygen to sulfur ratio (see supporting information), leading to a higher CB minimum.[58] In this device, the rollover effect is observed in illuminated JVT curves (Figure S10). The different JVT behavior in this device can be explained by a different CB alignment with the window (Al-doped ZnO) in this case (see supporting information). As we show in the following section, the rollover with the p^+ layer becomes only visible if a positive CBO at the B/W interface is present. Thus, we assume that the Cu-rich $CuInS_2$ absorber does contain a p^+ layer. However, the effect is only visible with the alternative buffer, which likely has a higher CBO at the B/W interface. This is a necessary condition for the rollover, as discussed in the following section.

5 | DEVICE SIMULATIONS

To check our explanations and to understand the observed JVT characteristics before and after HT, we perform numerical simulations using SCAPS-1D software.[59] The simulation parameters used for the device structure are given in Table 6. Where a range is given, the results of the parameter variation are discussed in the following. The parameters were optimized to match the unannealed Cu-poor $CuInSe_2$ device JV characteristics at room temperature. In the device, a series resistance of 0.3 Ω-cm^2 and flat band conditions at the back and front metal contacts are used throughout the simulations. Midgap neutral interface defects with density around 10^{15} cm^{-2} were also introduced at the p^+-$CuInSe_2$/CdS interface for the simulations.

Figure 11A shows the JV curve of the simulated device without the p^+ layer. The device has a CBO of +0.3 eV at the A/B interface, the buffer carrier concentration of 10^{17} cm^{-3} under illumination, and a buffer dark carrier concentration that varies from 10^{16} to 10^{17} cm^{-3}. We observe that by decreasing the carrier concentration of the buffer in the dark, the current of the crossover point also decreases. This shows that to have a crossover like observed in our devices (Figures 6, 10, and S7), the carrier concentration in the buffer should change considerably under dark and illumination conditions. Indeed, the impedance measurements performed by Werner et al.[33] on similar device structures show that the buffer conductance

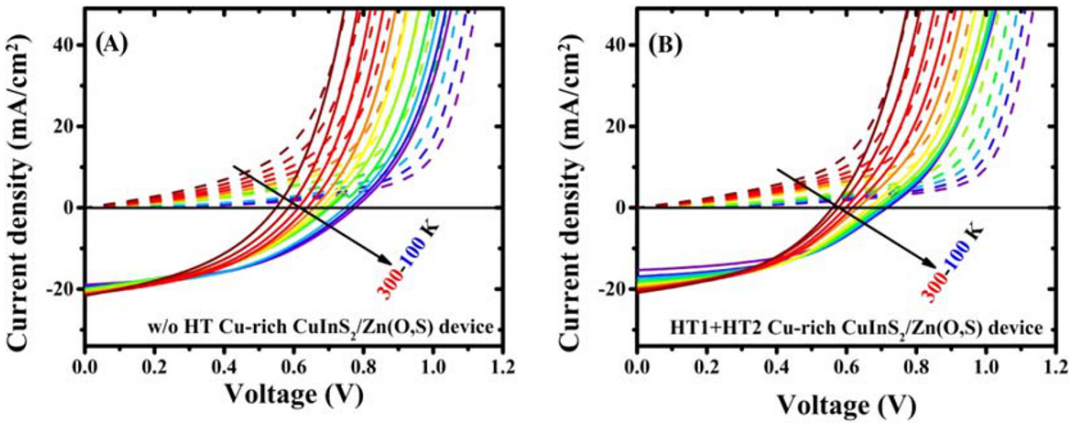

FIGURE 10 Temperature-dependent current–voltage curves of Cu-rich $CuInS_2$ device with Zn(O,S) buffer layer under dark and illumination condition (A) before HT and (B) after HT1 + HT2. HT, heat treatment [Colour figure can be viewed at wileyonlinelibrary.com]

TABLE 6 Simulation parameters used to simulated $CuInSe_2$ device with and without a defective p^+ layer

Parameter	$CuInSe_2$	p^+ $CuInSe_2$	CdS	i-ZnO	AZO
Thickness (μm)	2.5	0.1	0.060	0.080	0.220
Band gap (eV)	0.95	0.95	2.40	3.4	3.45
Electron affinity (eV)	4.6	4.6	4.3	4.6	4.55
Electron mobility (cm^2/Vs)	10	10	10	50	50
Hole mobility (cm^2/Vs)	5	5	2	20	20
Doping (1/cm^3)	1×10^{16}	1×10^{16}	$1 \times 10^{16-17}$	5×10^{17}	1×10^{20}
Defect density (1/cm^3) Single acceptor	1×10^{15} 300 meV	1×10^{15} 300 and 3×10^{16} 200 meV	-	-	-

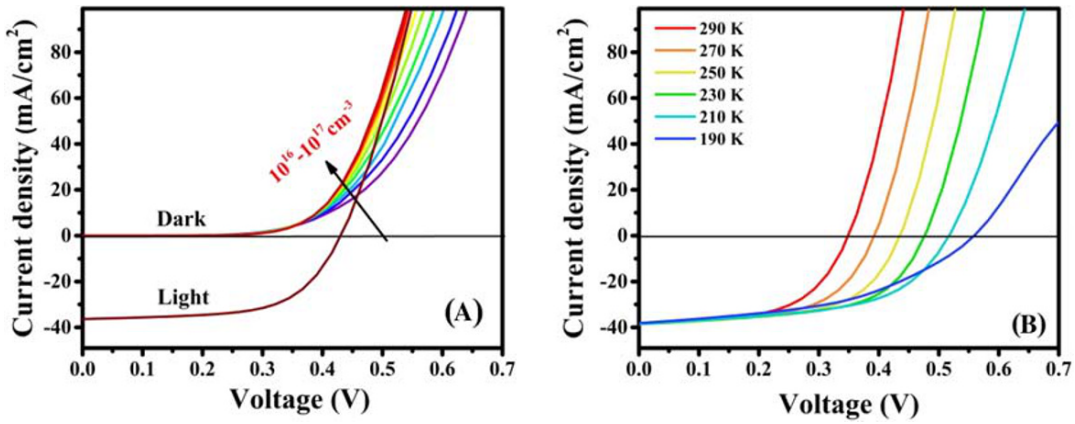

FIGURE 11 Simulated current–voltage curve without the defective p^+ layer (A) with varying dark carrier concentration in the buffer from 10^{16} to 10^{17} cm^{-3} (purple to red) keeping illuminated carrier concentration in buffer constant at 10^{17} cm^{-3}. (B) Illuminated curve at 300–200 K with the defective p^+ layer at the $CuInSe_2$ front surface. The rollover is observed clearly for the blue curve at moderate voltages ~0.6 V [Colour figure can be viewed at wileyonlinelibrary.com]

increases under illumination. The increase in conductance is due to increases in electron concentration in the buffer, which can be a result of direct electron generation in the buffer itself or injection of electrons from the absorber. Our JV measurements with red light favor the latter argument suggesting an increase of buffer conductance by injection of the electrons from the absorber.

The above model works very well for explaining the crossover in Cu-rich $CuInSe_2$, but to explain the rollover effect at lower temperatures, we need an additional barrier of some sort, which we introduce by adding a highly doped layer at the front in our Cu-poor device (the p^+ layer). The defect parameters of this layer were fixed by taking the experimental CV and admittance results (see supporting information) of Cu-rich devices into consideration. Figure 11B shows the simulations done with a p^+ at the front near the A/B interface. The parameters for this defective layer are reported in Table 6. For the blue curve, we can see a rollover at moderate voltage ~0.6 V. To ascertain the p^+ layer as the origin of the strong rollover, a device without the p^+ layer was simulated. Figure 12A shows the JVT curves of the device without the p^+ layer. The rollover that was observable for the device with the p^+ layer is not that obvious in this case. Finally, the JVT of the device with the p^+ layer but without the B/W offset is simulated. Unlike the first case, no rollover for this device was observed (Figure 12B). These simulations show that to explain the JVT curves as observed in our Cu-rich device (Figure 8), a p^+ layer in combination with B/W offset is needed.

There can be other causes of this kind of JVT behavior. For example, a back contact barrier or a difference in front contact barrier can also cause this rollover in the JV curve. However, we speculate that these might not be the main cause as both the Cu-rich and Cu-poor devices were made in the same deposition run for the buffer and the window. And if it is the back contact barrier, then one should also observe it in both Cu-rich and Cu-poor devices, because both types of absorbers were prepared at the same deposition temperature. Also, we do not think mild annealing such as in our case can change the back contact barrier so much, as the absorber processing temperatures are much higher than our annealing temperature. Hence, in our case, the model of the defective p^+ layer surface gives a more convincing explanation for our observations.

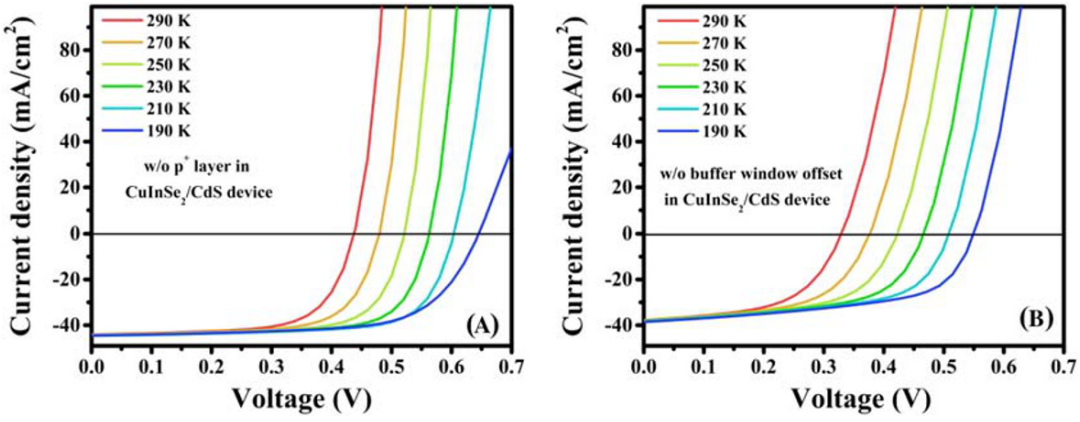

FIGURE 12 Simulated temperature-dependent current–voltage curves of $CuInSe_2$ device (A) without p^+ layer at the front keeping buffer/window offset −0.2 eV and (B) without buffer/window offset keeping p^+ layer in the structure [Colour figure can be viewed at wileyonlinelibrary.com]

6 | CONCLUSIONS

We have shown the impact of HT on solar cells made with $CuInSe_2$ and $CuInS_2$ absorbers grown with different compositions. In Cu-poor devices, HT reduces the non-radiative recombination. This reduction is confirmed by the increase in minority carrier lifetime, which leads to an increase in V_{oc} and qFls. However, after HT2, a decrease in doping concentration masks the positive effects of reduced non-radiative recombination, and as a consequence, the V_{oc} of the device remains unchanged.

In contrast, the Cu-rich devices suffer from low shunt resistance. No change in non-raditaive recombination is observed for the Cu-rich $CuInSe_2$ device, as the lifetime remains the same. Simultaneously, a decrease in doping after HT2 leads to the lowering of the qFls and the V_{oc} of the device. However, the majority of the V_{oc} loss originates from the poor shunt and degradation of contacts after HT2. A rollover in the device JV at low temperatures was observed and explained with the help of the p^+ layer. This p^+ layer was removed by HT2 due to reduced doping in this layer. Contrarily, changes in the Cu-rich $CuInS_2$ device performance after HT2 are fully explained by changes in the resistances. The effects of the p^+ layer in this device are only seen experimentally with an alternative buffer, with a higher CB maximum, where we can expect a non-zero CBO at the B/W interface.

In all the devices, the injection of electrons from the absorber into the buffer increases effective buffer doping, thus leading to a reduced barrier for electron injection and consequently leading to JV crossover in the devices.

In summary, the results presented here show how absorber composition can have a drastic influence on the effectiveness of post-deposition HT. Establishing the link between the absorber composition and material properties can be very crucial in understanding the impact of post-deposition treatments in complex material systems such as Cu (In,Ga)$(S, Se)_2$.

ACKNOWLEDGEMENTS

This contribution has been funded by Fonds National de la Recherche (FNR) Luxembourg in the framework of the Massena, Surpass, Curi-K and CORRKEST project, which is gratefully acknowledged. Moreover, we are thankful to Dr Marc Burgelman and his team at the University of Ghent, Belgium, for providing SCAPS-1D simulation software.

CONFLICT OF INTEREST

There are no conflicts of interest to declare.

ORCID

Mohit Sood https://orcid.org/0000-0002-2714-7737
Hossam Elanzeery https://orcid.org/0000-0001-6032-2499
Alberto Lomuscio https://orcid.org/0000-0002-3356-2486
Florian Werner https://orcid.org/0000-0001-6901-8901
Florian Ehre https://orcid.org/0000-0001-7711-6712

REFERENCES

1. Nakamura M, Yamaguchi K, Kimoto Y, Yasaki Y, Kato T, Sugimoto H. Cd-free Cu (In, Ga) (Se, S) 2 thin-film solar cell with a new world record efficacy of 23.35%. *46th IEEE PVSC*. 2019.
2. Hiroi H, Iwata Y, Adachi S, Sugimoto H, Yamada A. New world-record efficiency for pure-sulfide Cu (In,Ga)S_2: thin-film solar cell with Cd-Free buffer layer via KCN-free process. *IEEE J Photovolt*. 2016;6(3):760-763.
3. Polman A, Knight M, Garnett EC, Ehrler B, Sinke WC. Photovoltaic materials: present efficiencies and future challenges. *Science*. 2016; 352(6283):aad4424.
4. Kushiya K, Tachiyuki M, Kase T, et al. Fabrication of graded band-gap Cu (InGa)Se2 thin-film mini-modules with a Zn(O,S,OH)x buffer layer. *Sol Energy Mat Sol Cells*. 1997;49(1):277-283.
5. Hönes C, Hackenberg J, Zweigart S, Wachau A, Hergert F, Siebentritt S. A comparative study of the annealing behavior of Cu (In, Ga) (S, Se) 2 based solar cells with an indium sulfide buffer layer, partly submitted to wet chemical treatments. *J Appl Phys*. 2015; 117(9):094503.
6. Kushiya K, Hakuma H, Sano H, Yamada A, Konagai M. Effects of post-deposition heat treatments on ZnO/CdS/CuInSe2 thin film solar cells studied by photoluminescence measurements. *Sol Energy Mat Sol Cells*. 1994;35:223-229.
7. Kobayashi T, Yamaguchi H, Nakada T. Effects of combined heat and light soaking on device performance of Cu (In,Ga)Se2 solar cells with ZnS(O,OH) buffer layer. *Prog Photovolt*. 2014;22(1):115-121.
8. Kobayashi T, Jehl Li Kao Z, Kato T, Sugimoto H, Nakada T. A comparative study of Cd- and Zn-compound buffer layers on Cu (In1−x,Gax) (Sy,Se1−y)2 thin film solar cells. *Prog Photovolt*. 2016;24(3):389-396.
9. Khatri I, Matsuura J, Sugiyama M, Nakada T. Effect of heat-bias soaking on cesium fluoride-treated CIGS thin film solar cells. *Progr Photovolt Res Appl*. 2019;27(1):22-29.
10. Bär M, Ennaoui A, Klaer J, et al. The electronic structure of the [Zn(S,O)/ZnS]/$CuInS_2$ heterointerface—impact of post-annealing. *Chem Phys Lett*. 2006;433(1):71-74.
11. Gödecke T, Haalboom T, Ernst F. Phase equilbiria of Cu-In-Se. I. Stable states and non-equilibrium states of the In2Se3-Cu2Se subsystem. *Z Metallkd*. 2000;91:622-634.
12. Siebentritt S, Gütay L, Regesch D, Aida Y, Deprédurand V. Why do we make Cu (In,Ga)Se2 solar cells non-stoichiometric? *Sol Energy Mat Sol Cells*. 2013;119:18-25.
13. Choubrac L, Bertram T, Elanzeery H, Siebentritt S. Cu (In,Ga)Se2 solar cells with improved current based on surface treated stoichiometric absorbers. *Phys Status Solidi A*. 2017;214(1):1600482.
14. Turcu M, Pakma O, Rau U. Interdependence of absorber composition and recombination mechanism in Cu (In,Ga)(Se,S)2 heterojunction solar cells. *Appl Phys Lett*. 2002;80(14):2598-2600.
15. Elanzeery H, Melchiorre M, Sood M, et al. Challenge in Cu-rich CuInSe2 thin film solar cells: defect caused by etching. *Phys Rev Mat*. 2019;3(5):055403.
16. Jackson P, Wuerz R, Hariskos D, Lotter E, Witte W, Powalla M. Effects of heavy alkali elements in Cu (In,Ga)Se2 solar cells with efficiencies up to 22.6%. *Phys Status Solidi RRL*. 2016;10(8):583-586.
17. Carron R, Nishiwaki S, Feurer T, et al. Advanced alkali treatments for high-efficiency Cu (In, Ga) Se2 solar cells on flexible substrates. *Adv Energy Mat*. 2019;9(24):1900408.
18. Kato T, Handa A, Yagioka T, et al. Enhanced efficiency of Cd-free Cu (In,Ga)(Se,S)2 minimodule via (Zn,Mg)O second buffer layer and alkali metal post-treatment. *IEEE J Photovolt*. 2017;7(6):1773-1780.
19. Minemoto T, Matsui T, Takakura H, et al. Theoretical analysis of the effect of conduction band offset of window/CIS layers on performance of CIS solar cells using device simulation. *Sol Energy Mat Sol Cells*. 2001;67(1–4):83-88.
20. Lomuscio A, Rödel T, Schwarz T, et al. Quasi-Fermi-level splitting of Cu-poor and Cu-rich $CuInS_2$ absorber layers. *Phys Rev Appl*. 2019; 11(5):054052.

21. Hubert C, Naghavi N, Roussel O, et al. The Zn(S,O,OH)/ZnMgO buffer in thin film Cu(In,Ga)(S,Se)2-based solar cells part I: fast chemical bath deposition of Zn(S,O,OH) buffer layers for industrial application on co-evaporated Cu(In,Ga)Se2 and electrodeposited CuIn(S,Se)2 solar cells. *Progr Photovolt Res Appl*. 2009;17(7):470-478.
22. Maiberg M, Scheer R. Theoretical study of time-resolved luminescence in semiconductors. II. Pulsed excitation. *J Appl Phys*. 2014;116(12):123711.
23. Babbe F, Choubrac L, Siebentritt S. Quasi Fermi level splitting of Cu-rich and Cu-poor Cu (In, Ga) Se2 absorber layers. *Appl Phys Lett*. 2016;109(8):082105.
24. Niemegeers A, Gillis S, Burgelman M. A user program for realistic simulation of polycrystalline heterojunction solar cells: SCAPS-1D. Paper presented at: Proceedings of the 2nd World Conference on Photovoltaic Energy Conversion, JRC, European Commission, juli 1998.
25. Burgers A, Eikelboom J, Schonecker A, Sinke W. Improved treatment of the strongly varying slope in fitting solar cell IV curves. *Conference Record of the Twenty Fifth IEEE Photovoltaic Specialists Conference-1996*. 1996:569–572.
26. Johnson B, Korte L, Lußky T, Klaer J, Lauermann I. CuInS2–CdS heterojunction valence band offset measured with near-UV constant final state yield spectroscopy. *J Appl Phys*. 2009;106(7):073712.
27. Scofield JH. Effects of series resistance and inductance on solar cell admittance measurements. *Sol Energy Mat Sol Cells*. 1995;37(2):217-233.
28. Simsek Sanli E, Ramasse Q, Mainz R, et al. Evidence for Cu2–x Se platelets at grain boundaries and within grains in Cu (In, Ga) Se2 thin films. *Appl Phys Lett*. 2017;111(3):032103.
29. Schwarz T. A., Lomuscio SS, Gault B, Raabe D. On the chemistry of extended defects in CuInS2 films. Submitted. 2020.
30. Stephan C, Schorr S, Tovar M, Schock H-W. Comprehensive insights into point defect and defect cluster formation in CuInSe 2. *Appl Phys Lett*. 2011;98(9):091906.
31. Rau U, Braunger D, Schock H-W. Air-annealing effects on polycrystalline Cu (In, Ga) Se2 heterojunctions. Paper presented at: Solid State Phenomena 1999.
32. Niemegeers A, Burgelman M, Herberholz R, Rau U, Hariskos D, Schock HW. Model for electronic transport in Cu (In, Ga) Se2 solar cells. *Progr Photovolt Res Appl*. 1998;6(6):407-421.
33. Werner F, Siebentritt S. Buffer layers, defects, and the capacitance step in the admittance spectrum of a thin-film solar cell. *Phys Rev Appl*. 2018;9(5):054047.
34. Werner F, Babbe F, Elanzeery H, Siebentritt S. Can we see defects in capacitance measurements of thin-film solar cells? *Progr Photovolt Res Appl*. 2019;27(11):1045-1058.
35. Bastek J, Stolwijk NA, Wuerz R, Eicke A, Albert J, Sadewasser S. Zinc diffusion in polycrystalline Cu (In,Ga)Se2 and single-crystal CuInSe2 layers. *J Appl Phys*. 2012;101(7):074105.
36. Benabdeslem M, Benslim N, Bechiri L, Mahdjoubi L, Hannech EB, Nouet G. Diffusion of Zn in CuInSe2 bulk crystals. *J Cryst Growth*. 2005;274(1):144-148.
37. Hiepko K, Bastek J, Schlesiger R, Schmitz G, Wuerz R, Stolwijk NA. Diffusion and incorporation of Cd in solar-grade Cu (In,Ga)Se2 layers. *Appl Phys Lett*. 2011;99(23):234101.
38. Liao D, Rockett A. Cd doping at the CuInSe2/CdS heterojunction. *J Appl Phys*. 2003;93(11):9380-9382.
39. Ümsür B, Calvet W, Höpfner B, et al. Investigation of Cu-poor and Cu-rich Cu (In,Ga)Se2/CdS interfaces using hard X-ray photoelectron spectroscopy. *Thin Solid Films*. 2015;582:366-370.
40. Werner F, Bertram T, Mengozzi J, Siebentritt S. What is the dopant concentration in polycrystalline thin-film Cu (In,Ga)Se2? *Thin Solid Films*. 2017;633:222-226.
41. Werner F, Babbe F, Burkhart J, Spindler C, Elanzeery H, Siebentritt S. Interdiffusion and doping gradients at the buffer/absorber interface in thin-film solar cells. *ACS Appl Mater Interfaces*. 2018;10(34):28553-28565.
42. Persson C, Zhao Y-J, Lany S, Zunger A. n-type doping of CuInSe2 and CuGaSe2. *Phys Rev B*. 2005;72(3):035211.
43. Eisenbarth T, Unold T, Caballero R, Kaufmann CA, Schock H-W. Interpretation of admittance, capacitance-voltage, and current-voltage signatures in Cu (In, Ga) Se 2 thin film solar cells. *J Appl Phys*. 2010;107(3):034509.
44. Deprédurand V, Tanaka D, Aida Y, Carlberg M, Fèvre N, Siebentritt S. Current loss due to recombination in Cu-rich CuInSe2 solar cells. *J Appl Phys*. 2014;115(4):044503.
45. Maeda T, Wada T. First-principles studies on Cd doping in CuInSe2 and related compounds during chemical bath deposition of CdS buffer layer. *Jpn J Appl Phys*. 2013;52(6R):061201.
46. Unold T, Gütay L. Photoluminescence analysis of thin-film solar cells. *Adv Character Techniq Thin Film Solar Cells*. 2016;1:275-297.
47. Grimmeiss HG, Kullendorff N, Broser R. Photocapacitance studies of CdS:Cu. *J Appl Phys*. 1981;52(5):3405-3412.
48. Agostinelli G, Dunlop E, Bätzner D, et al. Light dependent current transport mechanisms in chalcogenide solar cells. *Proc 3rd World Conf Photovol Energy Conversion*. 2003;1:356–359 Vol.351.
49. Gloeckler M, Jenkins CR, Sites JR. Explanation of light/dark superposition failure in CIGS solar cells. *Mat Res Soc Symp Proc*. 2003;763.
50. Pudov AO, Kanevce A, Al-Thani HA, Sites JR, Hasoon FS. Secondary barriers in CdS–CuIn1−xGaxSe2 solar cells. *J Appl Phys*. 2005;97(6):064901.
51. Chung C-H, Bob B, Song T-B, Yang Y. Current–voltage characteristics of fully solution processed high performance CuIn(S,Se)2 solar cells: crossover and red kink. *Sol Energy Mat Sol Cells*. 2014;120:642-646.
52. Sze SM, Ng KK. *Physics of Semiconductor Devices*. Wiley-VCH Verlag GmbH & Co. KGaA: John wiley & sons; 2006.
53. Maciaszek M. Impact of the p+ layer on current–voltage characteristics of Cu (In, Ga) Se2-based solar cells. *J Appl Phys*. 2019;125(4):043102.
54. Scheer R, Schock H-W. *Chalcogenide photovoltaics: physics, technologies, and thin film devices*. Wiley-VCH Verlag GmbH & Co. KGaA: John Wiley & Sons; 2011.
55. Schulmeyer T, Kniese R, Hunger R, Jaegermann W, Powalla M, Klein A. Influence of Cu (In, Ga) Se2 band gap on the valence band offset with CdS. *Thin Solid Films*. 2004;451:420-423.
56. Säuberlich F, Fritsche J, Hunger R, Klein A. Properties of sputtered ZnO films and its interfaces with CdS. *Thin Solid Films*. 2003;431:378-381.
57. Mönig H, Lockhorn D, Aghdassi N, et al. Heat induced passivation of CuInSe2 surfaces: a strategy to optimize the efficiency of chalcopyrite thin film solar cells? *Adv Mater Interfaces*. 2014;1(2):1300040.
58. Kieven D, Grimm A, Lauermann I, et al. Band alignment at sputtered ZnSx O1–x/Cu (In, Ga) (Se, S) 2 heterojunctions. *physica status solidi (RRL)–Rapid Res Lett*. 2012;6(7):294-296.
59. Burgelman M, Nollet P, Degrave S. Modelling polycrystalline semiconductor solar cells. *Thin Solid Films*. 2000;361–362:527-532.

SUPPORTING INFORMATION

Additional supporting information may be found online in the Supporting Information section at the end of this article.

How to cite this article: Sood M, Elanzeery H, Adeleye D, et al. Absorber composition: A critical parameter for the effectiveness of heat treatments in chalcopyrite solar cells. *Prog Photovolt Res Appl*. 2020;1–14. https://doi.org/10.1002/pip.3314